J. Micromech. Microeng. **18** (2008) 104007 (10pp) doi:10.1088/0960-1317/18/10/104007

Passive water management for μfuel-cells using capillary microstructures

T Metz[1], J Viertel[2], C Müller[3], S Kerzenmacher[1], N Paust[1], R Zengerle[1] and P Koltay[1]

[1] IMTEK, Laboratory for MEMS Applications, Department of Microsystems Engineering, University of Freiburg, Georges-Koehler-Allee 106, D-79110 Freiburg, Germany
[2] IMTEK, Laboratory for Chemistry and Physics of Interfaces, Department of Microsystems Engineering, University of Freiburg, Georges-Koehler-Allee 103, D-79110 Freiburg, Germany
[3] IMTEK, Laboratory for Process Technology, Department of Microsystems Engineering, University of Freiburg, Georges-Koehler-Allee 103, D-79110 Freiburg, Germany

E-mail: koltay@imtek.de

Received 4 April 2008, in final form 24 July 2008
Published 29 September 2008
Online at stacks.iop.org/JMM/18/104007

Abstract
In this work we present a novel system for the passive water management in polymer electrolyte fuel cells (PEMFC) based on capillary effects in microstructures. The system removes abundant water that occurs at low temperatures at a fuel cell cathode and secures the humidity of the electrolyte membrane on higher temperatures. Liquid water is removed by hydrophilic gas supply channels with a tapered cross section as presented previously, and further transported by a system of capillary channels and a layer of nonwoven material. To prevent the membrane from running dry, a storage area in the nonwoven layer is introduced, controlled by a novel passive capillary overflow valve. The valve controls whether water is stored or finally disposed by gravity and evaporation. Experiments in a model system show that the nonwoven material is capable of removing all liquid water that can be produced by the fuel cell. A miniaturized fuel cell utilizing the novel water removal system was fabricated and experiments show that the system can stabilize the performance during changes of electrical load. Clearing the drowned miniaturized fuel cell flow field was proven and required 2 min. To make the capillary effects available for the originally hydrophobic graphite composite materials that were used to fabricate the flow fields, hydrophilic grafting based on photochemistry was applied to the material and contact angles of about 40° could be achieved and preserved for at least three months.

(Some figures in this article are in colour only in the electronic version)

1. Introduction

Water management is a key issue in the design of low-temperature polymer electrolyte membrane fuel cells (PEMFC). Water is essential as it enables the proton transport in the membranes and is part of the catalytic reactions [1]. Nevertheless, too much water blocks the oxygen supply at the cathode. In the low-temperature range (20 °C–65 °C), up to 95% of water is present in the liquid phase [2]. Water management systems in fuel cells have to prevent the cell from flooding and drying out.

Today's common approach is to remove abundant water by purging the cathode flow field and to pre-humidify the air. The purging requires a limited number of meandering channels pressurized by distinct pressure sources [3]. High flow rates and therefore pressure gradients are required to ensure a sufficient distribution of oxygen and humidity along the extended channels [4]. It has been shown, e.g. in [5], that long channels lead to inhomogeneous humidification conditions and a non-optimal power generation. The membrane can dry out at the beginning of the system and liquid accumulates at the channel ends. To recycle the water from the purging flow, a condenser is necessary.

In a conventional system the three components [1]: humidifier, cathode flow field and condenser require a large surface to volume ratio for the gas flow to perform the heat and water exchange. This comes along with a relatively large pressure loss and overall space requirements. In particular for miniaturized systems, it is preferable to use passive systems that (i) remove liquid without external actuation; (ii) do not require large pressure gradients; (iii) use only water produced during cell operation for humidification.

To meet these requirements, we consider a passive water management system that uses hydrophilic channels with a tapered cross section for the capillary water removal as presented in [6]. The channels allow for a parallel setup of the cathode flow field channels. Thus only moderate pressure gradients can be applied. Furthermore, condensation of water can take place inside the fuel cell without blocking the channels. A nonwoven layer is used for storage and disposal of water. Nonwoven material is used here as a synonym for fibrous porous material. In this work, a commercial cellulose tissue was used as nonwoven material. Together with small capillaries placed at the top of the flow field channels, it distributes condensed water all over the fuel cell and makes a humidifier obsolete.

Porous materials are already reported to be used for the removal and storage of water in PEM fuel cells. Perry *et al* [7] describe a passive water management system where the water in the cooling channels is connected by a porous flow field material to the cathode channels. It enables water removal and humidification by exchange of water between the channel systems. Nevertheless, in micro fuel cells, the application of cooling channels is mostly not applicable. Litster *et al* [8] combines porous materials with an osmotic pump, realizing active water management. In [9] a wick is used to internally store and redistribute water in a micro fuel cell. However, the channel system is not optimized for water removal and no final disposal of abundant water is provided.

In contrast to these approaches, the system presented in this work enables passively controlled passive water management by a combination of porous material and capillary microstructures. A novel capillary overflow valve is realized by a gap in the nonwoven layer and controls whether liquid is discharged or stored.

We discuss the working principle in theory and present results showing the functionality of the components in a model system as well as in experiments in a fuel cell.

2. Water production in fuel cells

In a PEM fuel cell, protons move through the polymer electrolyte membrane (PEM) from the anode to the cathode. In combination with oxygen, water molecules are formed (equation (1), [1]):

$$H_2 + \tfrac{1}{2}O_2 \longrightarrow H_2O + 286\ \text{kJ mol}^{-1}. \tag{1}$$

The mass flow of water $\dot{m}$ produced is a linear function of the current I and can be calculated from elementary numbers:

$$\dot{m} = \frac{I}{2\,e N_A} M_{H_2O} \tag{2}$$

$$\dot{m}_I = 5.6 \frac{\text{mg min}^{-1}}{A}. \tag{3}$$

In equation (3) M_{H2O} is the molar mass of water, e is the elementary charge and N_A is Avogadros number. The specific mass flow $\dot{m}_I$ is the mass flow produced by a current of 1 A. All water is produced at the cathode of the fuel cell.

Additionally there is a certain amount of water that is dragged from the anode to the cathode by the proton flux in the humidified membrane. Up to 2.5 molecules of water can be dragged per proton. Thus, the total mass flow of water occurring at the cathode can be up to five times higher than the water created according to equation (1)—providing enough water is available at the anode. The mass flow of water dragged through the membrane towards the cathode can be prevented by applying an overpressure of air at the cathode [1]. Without overpressure and with no explicit humidification of the fuel at the anode, only back diffusion through the membrane preserves the humidification of the anode. In this case a stable operation is possible but on a smaller performance level. This is often found in miniaturized systems where the humidification of the hydrogen at the anode is too costly [10]. At a stable load point, drag through the membrane is in equilibrium with back-diffusion; thus the total amount of liquid in the membrane is not changed. This case will be considered in this work.

The flow of air supplied at the cathode channels finally removes water from the fuel cell. The amount can be estimated by the total flux $\dot{V}$, the temperature T_{out} of the exhaust air and the saturation pressure $p_{sat}(T)$ of water in air. In equation (4) a water balance $\dot{m}_{water}$ as the difference between generated and removed water is set up (inlet temperature T_{in}, exhaust temperature T_{out}, pressure p, current I):

$$\dot{m}_{water} = I\dot{m}_I - \dot{V}\frac{p}{R_s \cdot T_{in}} \times 0.622 \frac{p_{sat}(T_{out})}{p - p_{sat}(T_{out})}. \tag{4}$$

An empirical function for the saturation pressure is given in [11],

$$p_{sat}(T) = \exp\left(\frac{c_1}{T} + c_2 + c_3 T + c_4 T^2 + c_5 \ln T\right) \quad \text{with}$$
$$c_1 = -6094.5; \quad c_2 = 21.125; \quad c_3 = -0.02745;$$
$$c_4 = 1.685 \times 10^{-5}; \quad c_5 = 2.458. \tag{5}$$

As an example, the values for a given load point of 150 mA cm^{-2} are calculated using equation (4) and the results are shown in table 1 for three different temperatures. Assuming a cell area of 2 cm^2 and a mass fraction of 50% water of a 50 μm thick MEA, a total amount of 5.8 μl of water would be stored inside the MEA. According to equation (4), at 70 °C all water would be removed in less than 2 min. This shows how difficult it is to set up a stable fuel cell system that is fed with dry air, as it is often required for miniaturized fuel cells.

Table 1. Water balance for different exhaust temperatures.

Temperature	30 °C	50 °C	70 °C
Water balance	1.2 μl min^{-1}	0.13 μl min^{-1}	−3.3 μl min^{-1}

Airflow, 15 ml min^{-1};T_{in}, 20 °C; cell area, 2 cm^{-2}; j, 150 mA cm^{-2}; p, 1 bar; R, 287 J kg^{-1} K^{-1}.

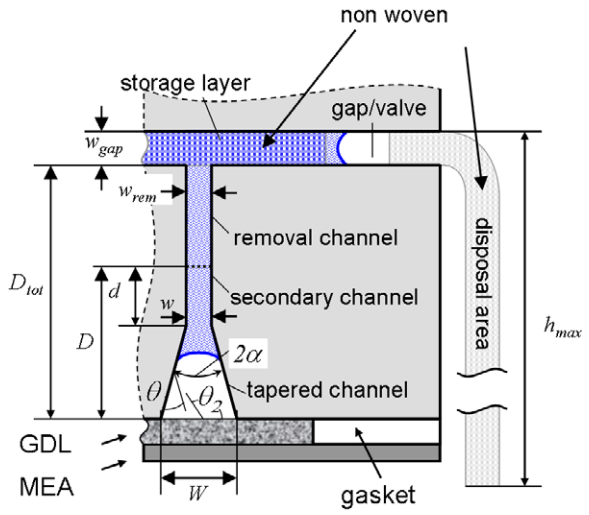

Figure 1. Cross section and parameterization of the passive water management system, integrated into the flow field.

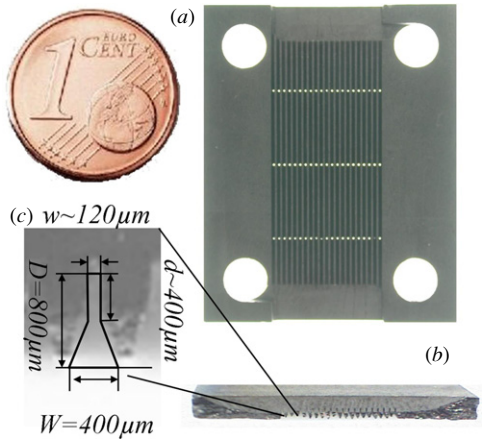

Figure 2. Photographs of the fabricated flow field: (*a*) top view, (*b*) cut along the removal channel, (*c*) enlargement of the tapered flow field channel.

3. Working principle

To deal with the challenges of water management, a passive capillary system is proposed. The system removes the liquid water that condenses during low-temperature operations of a fuel cell and stores it partially for rehumidification of the fuel cell at high temperatures.

The capillary system is integrated into the cathode flow field of a fuel cell as shown in figure 1. It consists of a number of capillary channels that realize transport of liquid water from the active area to the backside of the cathode flow field. Additionally, a nonwoven layer for the further transport out of the cell and the final disposal is introduced. The nonwoven layer also performs the water storage. The realized flow field is shown in figure 2.

In figure 3, the principle of the passive water management system is depicted as a chain of five capillary active features. The total pressure that drives the liquid from the cathode channel towards the capillary features is given by the channel pressure p_0 minus the capillary pressure p_{cap}:

$$p = p_0 - p_{cap}. \tag{6}$$

The channel pressure is the pressure applied for air supply at the cathode. The graph in figure 3 shows the principal pressure distribution in the system according to equation (6). It can be seen as the pressure gradient across a small water plug situated anywhere in the system. Such a plug would move from the higher to the lower pressure level whenever possible. In regions where the graph is flat, the water plug is at rest. When it grows and connects to a region with a lower capillary pressure it will move there until the pressure on both sides of the plug is equal again. Water follows the decreasing pressure along the path depicted in figure 3 out of the fuel cell as long as it is continuously removed in the disposal area. This can happen by gravity in a vertical column or evaporation. In the following sections all five capillary active features are discussed.

3.1. Flow field channels with a tapered cross section

The first of the five features in the capillary chain is the cathode flow field (figure 3 detail 1) that is built up from hydrophilic channels with a tapered cross section [6]. The narrow end of the channels profile is directed away from the MEA/GDL. In figure 4, the working principle is visualized by CFD simulations performed with a software package that accounts for free surfaces with surface tension and contact angle [12]. Droplets are lifted away from the MEA/GDL at the bottom into a secondary channel. This behaviour is denoted by the falling pressure ramp in figure 3 detail 1.

In [6], it is shown that the principle of droplet uplift works for any hydrophilic contact angle $\theta < 90°$. Some additional remarks on the role of the secondary channel will be given here: if the secondary channel is a self-priming open channel as discussed in [13], the liquid spreads along the channel and the droplets do completely vanish into it. This works as long as the following condition for the aspect ratio is fulfilled:

$$\frac{w}{d} < \frac{2\cos\theta}{1-\cos\theta}. \tag{7}$$

Once the secondary channel is liquid filled this end of the tapered channel is completely wetting.

On the other hand, a droplet spreads in the upper narrow end of the tapered section at least if the so-called Concus-Finn [14] condition for a half-opening angle α and a given contact angle θ, equation (8) is fulfilled:

$$\alpha + \theta < 90°. \tag{8}$$

Only if the droplets spread in the narrow end, the channel profile is decisively opened for the gas flow. For opening angles of $\alpha < 20°$, a contact angle as high as $\theta = 70°$ would be sufficient to fulfil equation (8). Now, as the wetted part of the secondary channel introduces an additional hydrophilic section into the edge, the droplets may spread even for higher contact angles than that proposed by equation (8). Nevertheless, in [6] it has been found that it is advantageous to have a large opening angle and small contact angles, resulting in a stronger capillary gradient to overcome contact angle

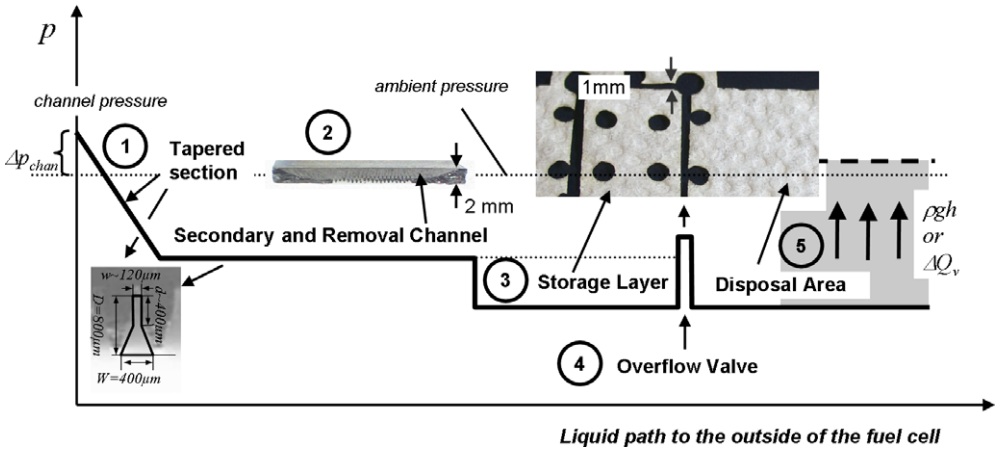

Figure 3. Schematic of the pressure distribution along the liquid path consisting of five elements. The liquid moves from left to right following the decrease in pressure.

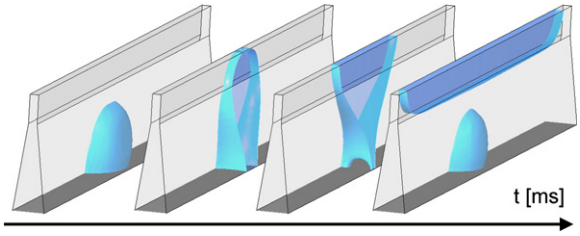

Figure 4. Simulation of droplets rising in the tapered channels using ESI-CFD ACE+.

hysteresis which under certain conditions prevents a droplet from moving upwards at all.

Channels, designed under these considerations, are safe against being clogged by liquid water and it is not necessary to design the flow field in a way that allows for purging (e.g., meandering channels). Parallel channels can be realized as has been done in this work (figure 2).

3.2. Secondary and removal channels

The next features are the secondary channel and the removal channel (figure 3 detail 2). These channels have a flat pressure characteristic in figure 3. Liquid spreads along the whole length of the secondary channel. This supports a homogeneous distribution of humidity in the fuel cell's flow field. To move the liquid water out of the flow field, the removal channels bridge the supply channels to the backside (figure 3 detail 2) of the flow field. The capillary pressure of removal and secondary channels must be equal to or higher than the capillary pressure of the tapered channels in the flow field. Because of the high aspect ratio the removal channels can be seen as slits and the capillary pressure p_{rem} can be calculated by their width w_{rem},

$$p_{\mathrm{rem}} = 2\frac{\sigma \cos\theta}{w_{\mathrm{rem}}}. \tag{9}$$

In the fabricated cell the width of the removal channels and the secondary channels is equal to $w = 120\ \mu$m. While not visible in figure 3, it is advantageous if the removal channels have a slightly smaller capillary pressure than the secondary channels. Thus the liquid is stored in the secondary channel where it is nearer to the active area to support humidification. The capillary pressure of the secondary channels can be calculated according to the divergence theorem [15]:

$$p_{\mathrm{cap,sec}} = 2\sigma \cos\theta \left(\frac{1}{w} + \frac{1}{2d}\right). \tag{10}$$

In equation (10) the depth of the channel still plays a minor role while in equation (9) it is neglected completely.

3.3. Nonwoven storage layer

The third element in the capillary chain is the storage layer. It is one part of a nonwoven layer at the backside of the cathode flow field. The other part of the nonwoven layer is the 'disposal area' which is placed partially outside the fuel cell.

A sufficient condition for the wetting of the porous material is that it is wetting at all $\theta < 90°$ and, together with its microstructure, has a higher capillarity than the secondary channel and the removal channel (figure 3 detail 3). In that case a liquid compartment that reaches from the removal channel to the storage layer is sucked into the storage layer. For the cellulose tissue used in this work, this fact was proven experimentally. Therefore, the contact angle and porosity were not determined explicitly.

3.4. Capillary overflow valve

The fourth element in the capillary chain is the capillary overflow valve. It is denoted in figure 1 by 'gap/valve'. Its functionality is explained in figure 5 (side view) in a simplified stratified setup (compare figure 1) that has been used to experimentally verify the working principle. The results are shown in figure 6 (top view). The overflow valve is realized by the gap dividing the nonwoven material in the storage layer (left in figures 5 and 6) and the disposal area (right in figures 5 and 6).

Water occurs in the flow field channel as droplets (figure 5(*b*)). The droplets are moved by the tapered section into the secondary channel and via the removal channel into the storage layer (figure 5(*c*)). At a certain moment, the storage layer is completely saturated with water. If still the

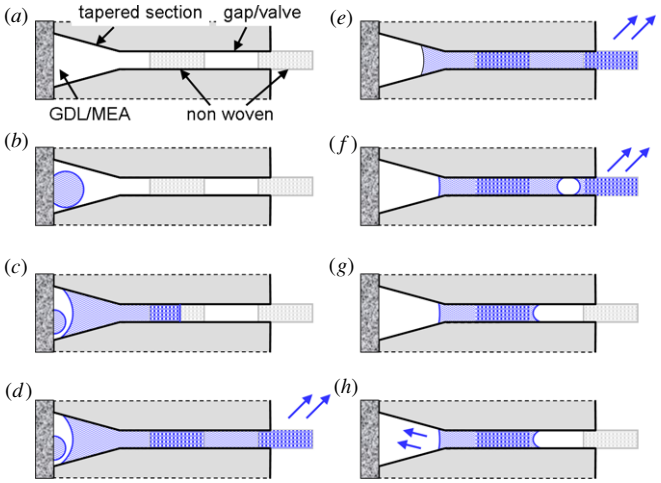

Figure 5. Schematic of the working principle of the capillary water management system in the cathode flow field and the overflow valve: (*a*) empty channel; (*b*) droplets occur at the top of the GDL; (*c–d*) liquid water is moved by the tapered channel and the nonwoven layer to the evaporation zone while a part of the channel remains open for gas flow; (*e–g*) no more water is generated, the overflow valve opens when the capillary pressure of the meniscus in the tapered section equals that of the gap; (*h*) the liquid in the storage layer and the secondary channels humidify the air in the cathode.

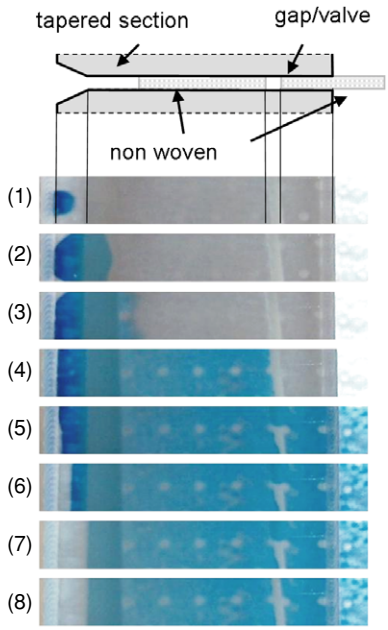

Figure 6. Movement of liquid in the model system. The tapered channel is on the left side. The disposal area on the right. From 1 to 6, the liquid in the tapered is moved from left to right, from the tapered section towards the disposal area. In 7 the tapered channel is empty and in 8 the overflow valve is cleared. ($\alpha = 30°$; gap length = 1.35 mm; $w = 200\ \mu$m; $D-d = 2.39$ mm.)

liquid appears in the tapered part of the flow field channels (figure 5(*d*)) it causes the overflow gap to become flooded and the liquid is transported into the disposal area. As soon as the flow field is cleared (figure 5(*f*)), the overflow valve disconnects the capillary chain. The water content in the storage layer is held back while the disposal area empties the overflow valve.

The height of the gap is equal to the thickness of the nonwoven layer and controlled by spacers. It must be larger than or equal to the width of the secondary channels in the flow field to ensure that the secondary channels are not cleared. In the realized design, conductive graphite spacers with a thickness of $w_{\mathrm{gap}} = 200\ \mu$m are used. The capillary pressure p_{gap} can be calculated analogue to equation (9). The length of the gap as the distance between the two nonwoven parts is about 1 mm.

The pressure stability of the overflow valve is essential in order to protect the fuel cell from running dry. As one can see from figure 3, the pressure stability of the overflow valve is given by the difference in capillary pressure between the gap and the secondary channel,

$$\Delta p_{\max} = 2\sigma \cos\theta \left(\frac{1}{w_{\mathrm{sec}}} - \frac{1}{w_{\mathrm{gap}}} \right). \tag{11}$$

The pressure stability as given in equation (11) must withstand the applied pressure drop on the cathode channels. Further it must withstand any thermo capillary pressure that can result from the thermal dependence of wetting conditions and surface tension as the temperature of the fuel cell interior and the environment differs. Assuming similar wetting conditions and the gap having double the width of the secondary channels, the pressure stability is about 50% of the capillary pressure in the secondary channels.

The maximum overpressure induced by the thermal change in surface tension can be estimated by the temperature gradients from the cathode channels towards the overflow valve. This may not be higher than 10 °C as the overflow valve is located at the backside of the cathode. Taking values for the surface tension of water from [16] for 70 °C (inside the cathode) and 60 °C (outside) the deviation in surface tension and therefore pressure is only 3%.

An antagonistic thermo capillary effect is the decrease of contact angle with temperature [17]. It would lead to a movement of the liquid into the fuel cell. Its effect depends strongly on the used materials and can be estimated to be small as well, at least for good wetting materials used in this work.

The absolute value for the pressure stability of the fabricated fuel cell should be 3.3 mbar according to equation (11) ($\theta = 40°$; $\sigma = 64.4$ m Nm^{-1} at 70 °C [16]). During the experiments, the cathode channel pressure at the inlet was measured constantly to be 1.4 mbar (±0.2 mbar). Thus it can be expected that the channel pressure did not lead to a liquid water drain out of the fuel cell.

3.5. Disposal area

The disposal area forms the fifth and final element in the capillary chain. It is built up from the outer part of the nonwoven layer (figure 3 detail 5) that is partly overhanging (figure 1). To finally remove the liquid, the pressure level must be raised above the ambient level in the removal area (figure 3 detail 5). This enables the liquid to leave the material against capillary forces. It can happen either through the pressure induced by gravity $p_{\mathrm{grav}} = \rho g h$ in the vertical part of the nonwoven layer or by evaporation with the latent heat ΔQ_v taken from the environment or the fuel cell. The latter

increases the pressure of the molecules towards the saturation pressure in the ambient air. Both processes work only in one direction—out of the fuel cell.

The gravity-induced pressure ensures the disposal of water even if evaporation is not sufficient. Once the nonwoven material is saturated and the gravitational pressure of the vertical liquid column overcomes the capillary pressure at the tip of the nonwoven material, liquid drips off. Experimentally the minimum necessary height for the material used was found to be 20 mm for dripping to occur.

4. Model system

4.1. Setup

As already shown in figure 1, the working principle has first been tested in a transparent model setup. The tapered channel was milled into the edge of the sample. The model consists of two plates of polycarbonate, clamped together by screws with the nonwoven layer in between. The contact angle of the material is about $70^\circ \pm 5^\circ$. The same graphite spacers that are used in the fuel cell are applied to define the height of the layer. The model system is a linear setup of the same features as used in the flow field (compare figures 1 and 5). The pictures of the liquid movement are shown in figure 6 (1–4). Liquid introduced in the tapered section at the edge of the sample spreads through the removal channel into the nonwoven storage layer (5). The overflow valve is flooded and the disposal area becomes wetted (5–7). After the inlet flow is stopped, the tapered section becomes cleared (8). The overflow valve disconnects and the capillary drain of liquid from the storage section is stopped as well.

4.2. Characterization of nonwoven material

The model system was used to characterize the water disposal by dripping for different nonwoven materials. The length of the overhanging disposal area was varied and average flow rates were calculated by the times necessary to clear the tapered section of the model system. The experiments were repeated several times with pre-wetted disposal areas. In all cases, at least 20 mm of the vertical length was necessary for the gravitational dripping to start. The dimensions in the model system, in particular the height of the nonwoven layers (200 μm) and the dimensions of the storage layer (15 mm $\times$ 25 mm), are similar to the fabricated fuel cell. The evaluated flow rates are depicted in figure 7. With increasing vertical length, the clearing time decreases as the flow rate increases. The reason is that the increasing length of the overhanging part comes along with an increasing gravitational pressure onto the droplet formed at the tip of the disposal area.

The flow rate q of water under the application of a gravity-induced pressure gradient is fitted against Darcy's law [18], that describes the pressure to flow ratio in porous materials. As the nonwoven layer inside the cell is squeezed, it has smaller pores and therefore a smaller permeability. Darcy's law was formulated for a combination of two sections with lengths l_1 and l_2 and permeabilities K_1 and K_2, the cross-sectional area of the channel, A, viscosity η and mass flow rate q:

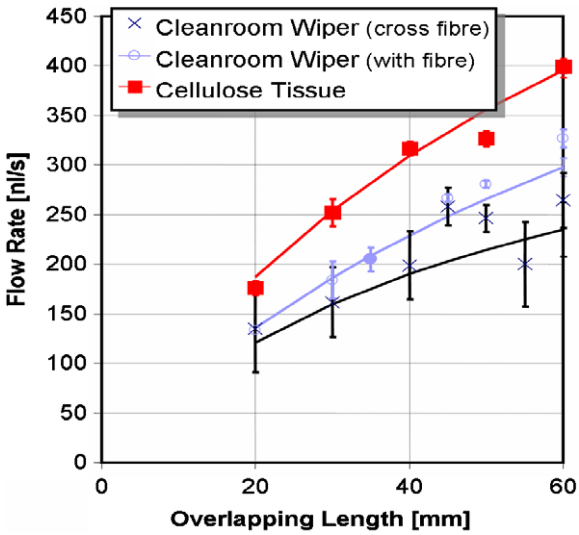

Figure 7. Experimental results and fitted curves for permeabilities of tissue.

Table 2. Values for the permeability of the nonwoven material, derived by fitting to Darcy's law.

Material	Outside K_2 (10^{-6} mm^3)	Inside K_1 (10^{-6} mm^3)
Clean room wiper (cross fibre)	0.15	0.07
Clean room wiper (with fibre)	0.25	0.07
Cellulose tissue	0.3	0.1

$$q = \frac{\rho g}{\eta} l_2 \left(\frac{l_1}{K_1} + \frac{l_2}{K_2} \right)^{-1} A. \tag{12}$$

The experimental data are fitted against equation (12), and the resulting parameters K_1 and K_2 are shown in table 2. The inner length l_1 was constant during the experiment at 25 mm. Two materials were investigated, cellulose tissue as used in the fuel cell and a clean room wiper with a strong fibre grading. The latter was tested with flow parallel to the alignment of the fibre grading ('with fibre') as well as with flow across the fibres alignment ('cross fibre'). From table 2 one can see that the cellulose tissue has the highest permeability. The permeability of the inner layer is reduced to one third of the permeability outside due to the squeezing. As expected, the permeability in the 'with fibre' alignment of the wiper is higher than that in the 'cross fibre' alignment. This is a known behaviour [20]. For the 'cross fibre' experiment, the decrease due to squeezing was less significant than for the with fibre experiment and the permeability of the squeezed part is nearly identical. The reason may be that the large spaces between the grading get closed during squeezing.

The width of the nonwoven layer was 15 mm in all experiments. From the results shown in figure 7, one can find that, e.g. with a disposal area of 50 mm length, 233 nl of liquid water per second and centimetre width can be removed from a distance of 25 mm towards the centre of the fuel cell cathode. This is the amount of water generated at the same area at a current density of 660 mA cm^{-2}. As the actual

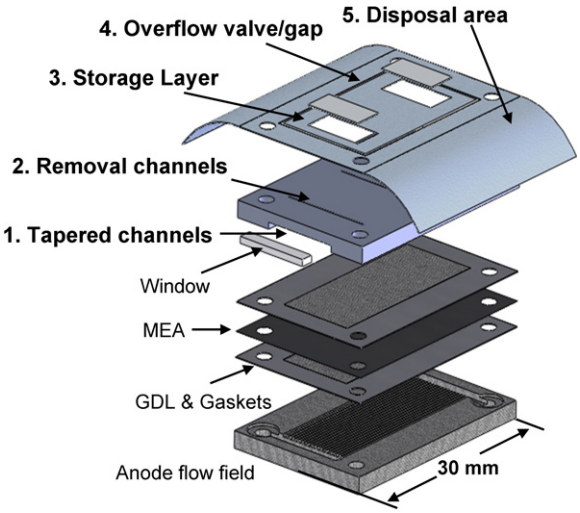

Figure 8. Design of the fabricated fuel cell utilizing the water management system.

dimensions of the fuel cell fabricated in this work are slightly smaller, the disposal should work in any case.

5. Fuel cell fabrication

The water management system was implemented into a fuel cell as depicted in figure 8. The designed total size of the active fuel cell area is 10×21 mm^2. For some experiments the area was reduced by larger gaskets to 8×14 mm^2 due to the fabrication requirements of the gaskets.

Cathode and anode flow fields (figure 3 detail 2) were milled into two conductive graphite composite materials: SIGRACET BMA4 [20] based on PVDF (polyvinylidene fluoride) and SIGRACET PPG 86 [21] based on PP (polypropylene). The cathode flow fields consist of 20 channels with a maximum width $w = 400$ μm at the GDL and a minimum width $w = 120$ μm at the secondary channel. The tapering angle of the channels was $2\alpha = 30^\circ$ and the maximum depth is $D = 800$ μm. The depth of the secondary channel is $d \sim 400$ μm. The secondary channels were fabricated by sawing with a circular saw blade. The tapered section was milled using a tapered tool. The cathode channels were closed by a transparent polymer window (800 μm $\times$ 10 mm).

The removal channels ($d = 1200$ μm, $w = 120$ μm) were sawn into the flow field from the backside. As a nonwoven material, cellulose tissue was used and the total liquid capacity of the storage layer at a height of 200 μm was measured gravimetrically to be 38 μl. The gaskets are cut out from 100 μm thick Teflon and the GDL consists of a 100 μm thick Teflon-treated Toray paper.

5.1. Surface treatment

As shown in our previous work [6] and repeated above, a major requirement of the tapered flow field channels for the removal of liquid water is a sufficient water wetting surface. As the original surface of the used materials (SIGRACET PPG 86, BMA 4) is hydrophobic ($\theta = 90^\circ$ to 105°), a hydrophilic surface treatment is required.

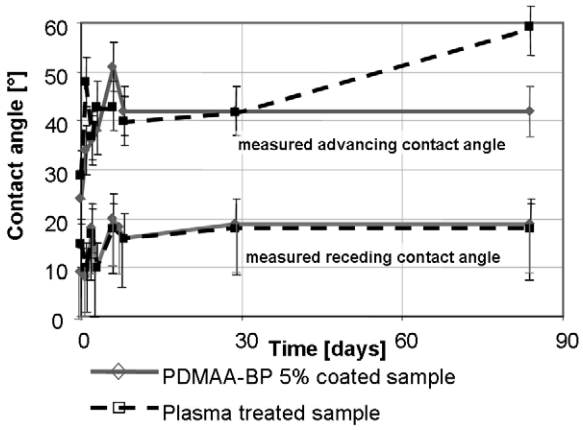

Figure 9. Advancing and receding contact angle measurements over three months of PPG 86 coated with PDMAA-MABP and plasma treated.

Therefore, a surface treatment with PDMAA-MABP (poly - (N, N -dimethylacrylamide-co-methacryloylbenzophenone)) was optimized to receive a stable hydrophilic coating of the flow field channels. Flat surfaces of one of the composite materials (SIGRACET PPG 86) were plasma treated with the O_2/H_2O -plasma for 4 min at 70 W. Afterwards, all samples except one were dip coated with PDMAA-MABP at different concentrations (5, 10 and 20 mg ml^{-1}) dissolved in ethanol with different molar parts of the benzophenone (BP) group (2%; 6%, 10%). The benzophenone groups were activated by exposure to UV light ($\lambda = 240$ nm; $t = 4$ min) to form a polymer network and to bind the hydrophilic PDMAA to the plasma-activated surface at the same time.

A useful contact angle was found only for one sample (5 mg ml^{-1} PDMAA-MABP with 6% MABP) and the one with pure plasma treatment. The other samples showed contact angles of $\theta = 80^\circ$ and higher. Now, multiple samples coated with the working mixture and contact angles were measured periodically over three months with increasing time intervals (figure 9). The advancing contact angles were stable at about $42^\circ \pm 5^\circ$ and the receding contact angles were situated at about 18° $+5^\circ/-10^\circ$ over the entire period. Contact angles below 20° were hard to detect and the error is relatively large. Even the sample (sample 21) that was only O_2/H_2O-plasma treated showed relatively good wetting properties over the whole period.

After ten weeks, the surfaces of the samples were investigated using x-ray photoelectron spectroscopy (XPS). An instrument from physical electronics was used (Physical Electronics 5600 ci, spot size 800 μm diameter, integration step 0.025 eV, integration time per step 100 ms). The peaks were grabbed and integrated with the local background neglected [22, 23]. In table 3 the weighted peak counts for oxygen and nitrogen are given by their ratio to the value for carbon and are compared to the theoretical ratios for PDMAA. The errors were taken as the deviation when integrating only over the half width of the peak. Compared to the untreated reference sample (nr. 23), an increased amount of nitrogen and oxygen was found on one of the samples coated with PDMAA-MABP (nr. 20) while on the plasma only treated sample (nr. 21) a significant increase in oxygen was observed.

Table 3. Ratios in spectral peaks from XPS measurements.

Nr.	Type	Oxygen/carbon	Nitrogen/carbon
20	O_2/H_2O-plasma & PDMAA-MABP dip coated	0.96 ± 0.07	0.14 ± 0.04
21	O_2/H_2O –plasma only	1.15 ± 0.24	0.06 ± 0.01
23	Pure material (PPG 86)	0.56 ± 0.1	0.06 ± 0.01
	Theoretical PDMAA layer	0.2	0.2

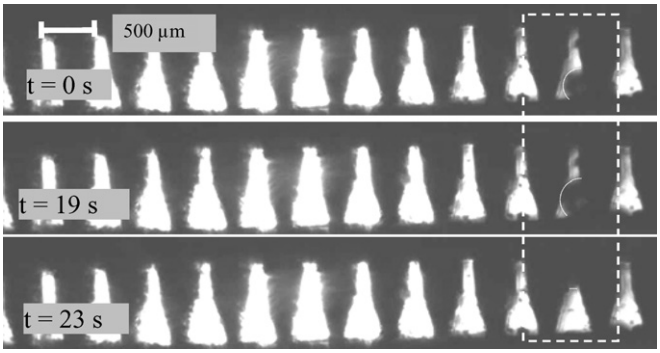

Figure 10. Photographs of the cathode during operation ($j = 133$ mA cm^{-2}). A droplet grows and moves upwards.

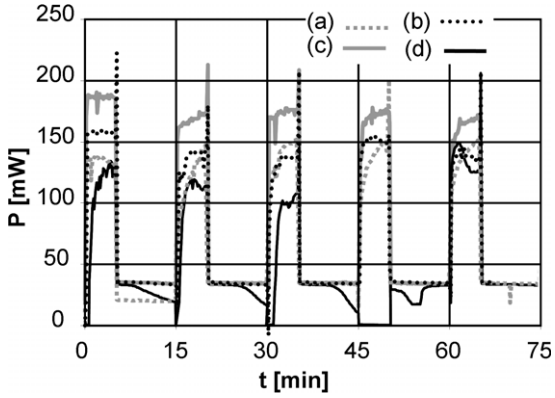

Figure 11. Performance during load cycling ($j_{min} = 45$ mA cm^{-2}; $j_{max} = 266$ mA cm^{-2}; airflow = 30 ml min^{-1}; $T = 55$ °C; 1.12 cm^{-2}). Setup variations: (*a*) complete; (*b*) no overflow valve; (*c*) no storage layer; (*d*) rectangular channels.

As nitrogen is a characteristic element of the PDMAA molecule, its presence indicates that a layer of PDMAA was successfully applied to sample 20 and was still present after ten weeks. The high oxygen content can only result from the O_2/H_2O-plasma treatment and indicates that the low contact angle of the sample is a result of it. This is remarkable as the O_2/H_2O-plasma on standard plastic surfaces typically lead to small contact angles that are stable only for one or two weeks. The reason may lie in the microstructure and the chemistry of the composite material which is not disclosed to the authors. Further the oxygen content was much higher and the nitrogen much smaller than one would expect for a full cover of PDMAA. This indicates that due to the fine structure of the composite, the PDMAA might not build a smooth and closed film. For the fuel cell fabrication, the PVDF-based graphite composite SIGRACET BMA4 was successfully coated with PDMAA-MABP (5 mg ml^{-1} with 6% MABP) as well.

6. Fuel cell experiments

6.1. Water removal

In the first step, a single micro fuel cell was assembled with the described flow field. The transparent window, that seals the front of the cathode channels, allows for the observation of the growth and removal of water along the cathode channels. As found in [6], the droplets were growing at the MEA/GDL and lifted into the secondary channel as soon as they touched both channel walls (figure 10). After several minutes of operation, the removal area was wetted and the liquid was disposed by evaporation. In order to investigate the clearance behaviour of a completely drowned fuel cell, water was artificially brought into the cathode flow field with a syringe through the air inlets. After the complete flow field was drowned with water, it cleared itself within 2 min by the capillary forces.

Table 4. Water production rate at different load points.

Current density (mA cm^{-2})	45	45	266	266
Water saturation in exhaust air (%)	100	30	100	30
Water balance (μl min^{-1})	−3.9	−1.0	−2.4	+0.5

Airflow, 30 ml min^{-1}; cell area, 1.12 cm^{-2}; T_{in}, 20 °C; T_{out}, 55 °C; p_0, ambient; R, 287 J kg^{-1} K^{-1}

6.2. Stability against drying out

Furthermore the beneficial effect of the new design to prevent the MEA from running dry was studied. The cell was operated with a surplus of dry air while a periodic switching between two different load points ($j_{min} = 45$ mA cm^{-2}, $j_{max} = 266$ mA cm^{-2}) was performed. The fuel cell temperature was kept constant at 55 °C ± 2 °C. In table 4, the theoretical water production rate according to equation (4) is shown for the two load points. Though the cell is nearly in equilibrium for the higher load level, in both cases, a drain of water would be expected at least for the lower load level. When calculating with a water saturation of 100% of the exhaust air, one can see that even for the higher load level the cell should dry out. At a smaller relative water saturation of the exhaust air of e.g. 30%, enough water is generated to humidify the fuel cell independent of the channel geometry (fourth column of table 4).

In figure 11, the measured performance over time for four varying cell setups is shown. The higher load point was applied for 5 min and the lower load point for 10 min.

Setup (a) is the complete flow field design as given in figure 8, with all described capillary features. In setup (b),

no overflow valve was present and the nonwoven material consists of only one section. In setup (c), the nonwoven material was not present at all and thus, no final disposal of water was possible for the cell. Setup (d) was built up using parallel hydrophobic rectangular channels (20 channels, 300 × 300 μm^2) as typically used in fuel cells.

In figure 11 a certain decline of the fuel cell performance can be observed when utilizing the rectangular channels. It happens in every cycle for about 5 min after switching to the lower load point (black graph). For an assumed water content of the MEA of 5 μl, this would agree well with the calculated water removal rate of 1 $\mu l\ min^{-1}$ (table 4) for the assumed water saturation of 30% in the exhaust air. At least the timescale of several minutes for drying out of the MEA fits well. Further it can be found in figure 11 that by using the common rectangular channels the higher performance level is not always recovered. This must be a result of an overall water removal from the MEA after a certain number of load cycles. The recovery of the performance after the fourth high load period results from the current driven setup, that forces water production even if the performance declines completely towards zero as water production is only a function of the current.

In contrast to the performance graph of the rectangular channels, the performance graph for all variations of the novel channel design follows the applied load changes in a quite stable way. This indicates that the stored water in the capillary system stabilizes the micro fuel cell against load changes. Nevertheless, in these experiments no significant difference was found between the different setups. This suggests that the storage of water in the secondary channels (total volume 20 μl per flow field) is already large enough to stabilize the fuel cell in the performed experiments over the period of 10 min of reduced water production. This is reasonable as the water available in the secondary channels is nearest to the MEA and is accessible all along the channels. Therefore it is most convenient for humidifying the MEA. According to equation (4), a temperature change or a change in the air supply rate between different stationary points has a similar impact on a fuel cell water household as a change in the current density has. Thus, it can be assumed that the stabilization effect can also be observed for temperature variations or changes in the air supply rate.

7. Conclusion and outlook

A novel system for the passive water management in miniaturized fuel cells was proposed, tested and successfully implemented in a test cell. The removal of water, using channels with a tapered cross section, was observed. Experiments indicate that the system is able to stabilize the fuel cell against running dry for short periods of reduced water production. Such droughty periods can result from different changes in the operating conditions of a fuel cell (temperature, humidity, gas flow or load) and were modelled successfully by load changes. The comparison of the performance behaviour of the different cell setups indicate that already the secondary channels at top of the tapered cathode channels store a sufficient amount of water to keep the cathode air humidified for about 10 min of reduced water production.

It was found that the nonwoven material as used in this work can remove liquid water sufficiently from miniaturized fuel cells. The final removal of liquid can not only be performed by evaporation but also by gravity-induced dripping from a vertical layer of a few centimetres length. Nevertheless such a wick must be designed carefully, e.g. according to the considerations made in this work. The disposal by dripping will reach a limit for larger cells as the squeezed part of the nonwoven layer increases with the MEA area to be cleared that leads to a reduced overall permeability of the layer.

For the fabrication of flow fields, a novel fabrication route by sawing of high aspect ratio micro channels was used. A hydrophilic surface coating, based on photochemical linkage of PDMAA-BP was applied to the PP and PVDF-based graphite composite materials. The coating led to sufficient contact angles ($\theta < 40^\circ$), stable at least over a period of three months. A remarkable result is the relatively long termed stability of O_2/H_2O plasma hydrophilic coating on the PP-based graphite composite material. A contact angle of about 40° was realized that increased only towards 60° over the whole period. The reason must lie in the micro to nanostructure of the composites surface and its specific chemistry.

The presented capillary overflow gap provides a novel design principle that enables a controlled liquid release. It can be used in other micro fluidic systems as well. In future designs the nonwoven material as used in this work can be substituted by microstructures with the advantage to be more controllable and to allow for higher flow rates. It should also be possible to further develop capillary structures to directly guide water from the cathode to the anode to compensate for the water drain induced by the proton flux. This would allow for compact, miniaturized fuel cell designs with high-integrated flow fields in the future.

References

[1] Vielstich W, Lamm A and Gasteiger H 2003 *Handbook of Fuel Cells—Fundamentals, Technology, Applications (Fundamentals and Survey of Systems* vol 1*)* (New York: Wiley)

[2] Tüber K 2004 *Analyse des Betriebsverhaltens von Polymer-Elektrolyt-Membran-Brennstoffzellen für portable Systeme* (Essen: Universität Duisburg-Essen)

[3] Nguyen N T and Chan S H 2006 Micromachined polymer electrolyte membrane and direct methanol fuel cells—a review *J. Micromech. Microeng.* **16** R1–12

[4] Zhang F Y, Yang X G and Wang C Y 2006 Liquid water removal from a polymer electrolyte fuel cell *J. Electrochem. Soc.* **153** A225–32

[5] Wang Y and Wang C Y 2006 Ultra large-scale simulation of polymer electrolyte fuel cells *J. Power Sources* **153** 130–5

[6] Metz T, Paust N, Müller C, Zengerle R and Koltay P 2007 Passive water removal in fuel cells by capillary droplet actuation *Sensors Actuators* A **143** 49–57

[7] Perry M and Kotso S 2004 A back-up power solution with no batteries *26th Ann. Int. Telecommunications Energy Conf., INTELEC 2004* pp 210–7

[8] Litster S, Buie C R, Fabian T, Eaton J K and Santiago J G 2007 Active water management for PEM fuel cells 5 *J. Electrochem. Soc.* **154** B1049–58
[9] Ge S H, Li X G and Hsing I M 2005 Internally humidified polymer electrolyte fuel cells using water absorbing sponge *Electrochim. Acta* **50** 1909–16
[10] Muller M, Muller C, Gromball F, Wolfle M and Menz W 2003 Micro-structured flow fields for small fuel cells *Microsyst. Technol.* **9** 159–62
[11] Sonntag D and Heinze D 1982 *Sättigungsdampfdruck- und Sättigungsdampfdichtetafeln für Wasser und Eis* vol 1 (Grundstoffindustrie: VEB Deutscher Verlag)
[12] ESI-Group 2006 CFD-ACE+ 2007
[13] Jokinen V and Franssila S 2007 Conditions for capillary filling in microfabricated channels with hydrophilic and hydrophobic walls *Proc. μTas Conf. (Paris, France, 2007)* pp 367–9
[14] Concus P and Finn R 1974 Capillary free surfaces in absence of gravity 1 *Acta Math.* **132** 177–98
[15] Langbein D 2002 *Capillary Surfaces: Shape, Stability, Dynamics, in Particular Under Weightlessness* (Berlin: Springer)
[16] Nguyen N T and Wereley S T 2002 *Fundamentals and Applications of Microfluidics* (Boston: Artech House)
[17] Brochard F 1989 Motions of droplets on solid-surfaces induced by chemical or thermal-gradients 13 *Langmuir* **5** 432–8
[18] Sigloch H 1996 *Technische Fluidmechanik* (Düsseldorf: VDI Verlag)
[19] Volkov V A, Bulushev B V and Ageev A A 2003 Determination of the capillary size and contact angle of fibers from the kinetics of liquid rise along the vertical samples of fabrics and nonwoven materials *Colloid J.* **65** 523–5
[20] Eisenhuth 2004 SIGRACET Bipolar Plate BMA 4 *Product Datasheet*
[21] Eisenhuth 2004 SIGRACET Bipolar Plate PPG 86 *Product Datasheet*
[22] Seah M P 1981 A quantitative framework for the analysis of surfaces by Aes and Xps 6 *Analusis* **9** 171–80
[23] Chastian J and King R C 1995 *Handbook of X-Ray Photoelectron Spectroscopy—A Reference Book of Standard Spectra for Identification and Interpretation of XPS Data* (Eden Prairie, MN: Physical Electronics Inc.)